An advanced resin reaction modeling using data-driven and digital twin techniques

Chady Ghnatios, Pierre Gérard, Anais Barasinski

Noname manuscript No.
(will be inserted by the editor)

An advanced resin reaction modeling using data-driven and digital twin techniques

Chady Ghnatios* · Pierre Gérard · Anais Barasinski

Received: date / Accepted: date

Abstract Elium® resin is nowadays actively investigated to leverage its recycling ability. Thus, multiple polymerization modeling are developed and used. In this work, we investigate the polymerization of Elium®/Carbon fiber composite in a cylindrical deposition, followed by an in-oven heating. The model parameters are optimized using an active-set algorithm to match the experimental heating profiles. Moreover, the simulation efforts are coupled to an artificial intelligence modeling of the discrepancies. For instance, a surrogate model using convolution recurrent neural network is trained to reproduce the error of the simulation. Later, a digital twin of the process is built by coupling the simulation and the machine learning algorithm. The obtained results show a good match of the experimental results even on the testing sets, never used during the training of the surrogate model. Finally, the digital twin results are post-processes to investigate the resin polymerization through the thickness of the part.

Keywords Digital twin · Elium® · polymerization · composite material

1 Introduction

Thermoplastic Composite materials have proven to be a viable engineering solution for a wide range of applications requiring high performance compo-

C. Ghnatios
Corresponding author.
Notre Dame University-Louaize, Department of mechanical engineering, Zouk Mosbeh, PO Box 72, Lebanon. E-mail: cghnatios@ndu.edu.lb

P. Gérard
Groupement de Recherche de Lacq, Arkema, Route Departementale 817, BP 34, 64170 Lacq, France.

A. Barasinski
Universite de Pau et des Pays de l'Adour, E2S UPPA, CNRS, IPREM, Pau, France. E-mail: anais.barasinski@univ-pau.fr

nents [1,2]. With increased interested in their applications with the arrival of the electric vehicles, developing composite materials with the aim of reducing energy consumption represents a challenge for years to come. Indeed, the possibilities offered by these materials are appealing since they offer an incredible ratio of mechanical performance to density, and they can easily be endowed with special properties, multiple functionality, and even gradient properties in a wide range of applications. Recently, thermoplastics are aimed as they potentially offer the possibility of being completely recycled [3,4]. Another advantage over metal alloys is the ability to design components with properties tailored to a specific application. Composed of two macroscopically separate materials, the reinforcement and the matrix, whose different characteristics together contribute to the final properties. Composite components offer additional design freedom that allows them to be engineered to withstand a variety of loads and working conditions while having more efficient functional configurations [5]. This freedom comes from the ability to manipulate processing variables such as fiber orientations of sequentially stacked layers or fiber volume fractions. Because of this advantage, composite materials are particularly relevant to the transportation sectors and play an important role in the current and future success of these industries. However, today, if the applications using these materials are more and more numerous, they are not up to what one could expect, neither in quantity, nor in quality, with production rates often limited [6].

One of the critical aspects to enhance remains the composite materials manufacturing processing time, especially to be in phase with the needs of the automotive industry. Facing such challenge, reactive resin solutions have been proposed [1]. In fact, these resins allow to guarantee a low viscosity of the material during its implementation, and concentrates during the process the polymerization and consolidation phase, thus offers the possibility to reduce drastically the processing time [7]. This solution is very attractive, guaranteeing an ease of implementation similar to thermosetting resins, shortening the operations on the products, and decreasing the number of processing operations, which is also a considerable gain from the energy point of view [7].

The down-side of these solutions is that the complex manufacturing process, a key to delivering high performance parts, is not mastered yet. An inadequate control of the polymerization step leads to reduced mechanical properties, and final performance not matching expectations [8,9]. Thus, few industries today take the step of using these reactive systems, which concentrate all the final properties of the part in a single step of implementation.

On a parallel line to these technological advances in polymer design, the digital world has evolved and Industry 4.0 has brought solutions for a better modeling and control of industrial processes. Novel modeling and simulation methods are combining the modern computation tools with artificial intelligence algorithm to enhance their prediction ability [10]. While using machine

learning is a trend in computational mechanics [11–15], these models tend to violate basic engineering principles. Therefore, new techniques based on satisfying basic principles appeared [16–18]. Others preferred to update the simulation reduced basis subspace using experimental measures and experimental variability, while constraining the variation into the physical manifold of the problem [19–22], constructing therefore a stochastic digital twin of the measured instance. Digital twins, also known as hybrid twins, is a novel paradigm in computational mechanics, where data complements the simulation to tackle the possibility of generating highly predictive and physics-based realistic solutions [23–25].

In this work, we propose to build a digital twin for the curing of one of the popular reactive resin known as Elium, using a deterministic modeling as measurements of the experimental variability are not available. Deterministic digital twins deliver an enhanced predictive simulation through a correction of the simulation results, while conserving the physical interpretability of the results. This work is part of this issue, how to give confidence to users of reactive resins, so that they control the processing throughout the day, and in particular ensure that the polymerization reaction, generally exothermic, does not cause hot spots, which would irreversibly damage the material, and guarantee a maximum rate of polymerization, and therefore mechanical properties expected at the end of the part manufacturing. Moreover, this work generates a $3D$ map of the polymerization ratio, as a function of the selected heating cycle, something unavailable by any other means nowadays. The map can be generated post curing, using experimental data, or estimated pre-curing using the built model as an integrator scheme.

In the first part, of the work, section 2 reviews the main materials and methods used for the measurements of the data, while section 3 explore the obtained experimental results. In section 4, we explore the simulation model used in this work, which is enhanced in section 5 using machine learning techniques. Finally, the obtained digital twin results are shown in section 6 and some conclusions are drawn in section 7.

2 Materials and method

2.1 Materials

Composites tanks were made from continuous carbon fiber, impregnated by a winding grade monomer formula, Elium®C595 of Arkema, France. The tanks winding process prior to curing is illustrated in figure 1.

2.2 Manufacturing

Six composites wounded structures made of 92 plies were manufactured, on a cylindrical drum. The main material parameters are the same for all six

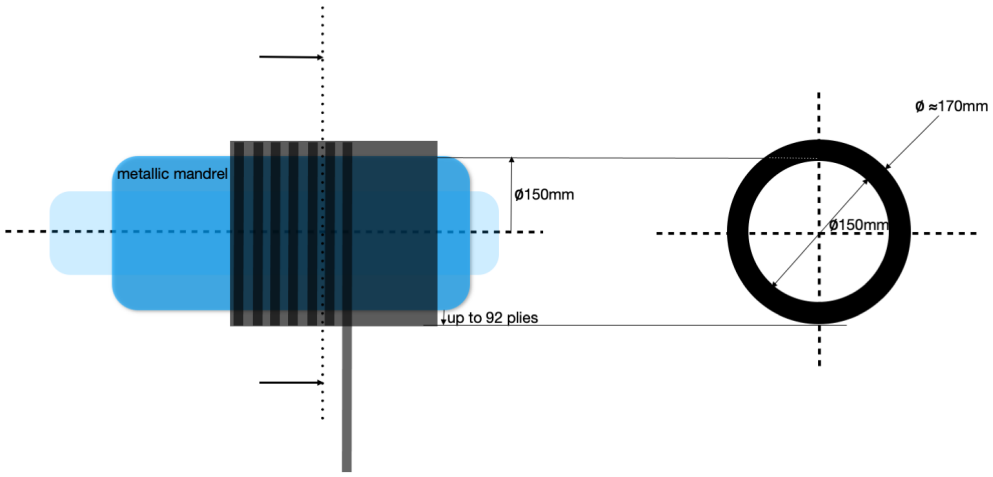

Fig. 1: Winding process.

experiments, the curing cycles are slightly different. The first step being the impregnation and winding, at ambient temperature, followed by a second step performed in an oven consisting in a temperature cycle of 1h at 80°C to perform the polymerization of the matrix. During this polymerization phase, the temperature is recorded within the structure thanks to 3 K-type thermocouples placed at the interface of plies 1/2, 45/46, and 91/92. An additional thermocouple allows the following of the environment temperature inside the oven cavity being the unique controlled input, it will be noticed T_∞ in the furthur modeling of the process . The schematic of the deposited composite material is illustrated in figure 2.

3 Experimental results

Six experimental polymerization data are available with the initial composite material. The simulation will however consider only the main heating phase, where the main resin polymerization process occurs. The experimental measurements are shown in figure 3 for two selected cases, in figure 3(a), and figure 3(b).

The experimental data sets are used with the environmental temperature as an input for the simulation. The convection coefficient are previously identified internally and found to be at $r = R_{max}$ is $h_{out} = 50W/m^2.K$, while the one at the inner part of the drum, $r = R_{min}$ is $h_{in} = 2W/m^2.K$. Obviously, inside the cylindrical support, the convection is hindered by the small inner diameter of the cylinder, reducing naturally the air circulation inside the used hollow shaft.

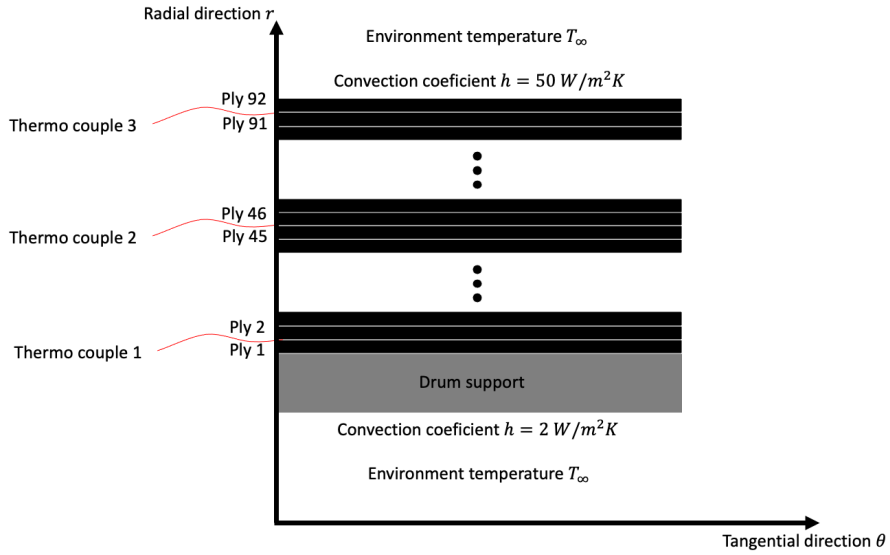

Fig. 2: The schematic of the studied deposition.

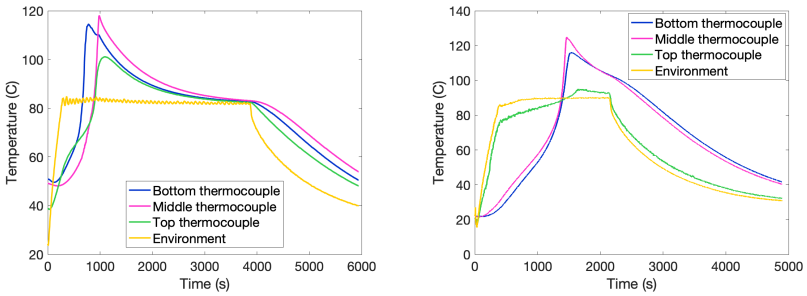

(a) Sample data from an experiment

(b) Other example of an experiment sample data

Fig. 3: The thermocouple and environment temperature data for two selected experiments. In correlation with figure 2, the bottom thermocouple refers to the thermocouple 1, the middle thermocouple is the one thermocouple 2 and the top thermocouple is the thermocouple 3.

4 Resin polymerization model and simulation

Resin polymerization model published in [26] is initially considered, while using cylindrical coordinates. For instance, leveraging the axisymmetrical shape and boundary conditions, and neglecting the edge effects, the thermal fields are modeled using the transient 1D cylindrical heat transfer equation with heat

generation:

$$\frac{\partial T}{\partial t} - \frac{1}{r}\frac{\partial}{\partial r}\left(\mu r \frac{\partial T}{\partial r}\right) = Q \tag{1}$$

T denotes the thermal field, t the time, r the radial coordinate, μ the thermal diffusivity and Q the heat generation therm.

Q is modeled initially using the resin polymerization model in [26]. Its expression is the following :

$$Q = -\frac{\Delta H}{C_p M_w^0 M_0}\frac{dM}{dt} \tag{2}$$

with ΔH being the total enthalpy of polymerization, C_p the heat capacity of the composite material, M the concentration of monomer, M_0 the initial concentration of monomer at $t = 0$ and M_w^0 the molecular weight of the monomers. The monomer used in this work in the methyl methacrylate (MMA). The heat capacitance of the composite material is homogenized using the law of mixture [27] as follows:

$$C_p = (1 - w_f)\left((1 - \mathcal{X})C_{p,m} + \mathcal{X}C_{p,p}\right) + w_f C_{p,f}, \tag{3}$$

with w_f the fibers mass fraction, $\mathcal{X}$ the degree of monomer conversion, $C_{p,m}$ the monomers heat capacity, $C_{p,p}$ the polymer (polymethyl methacrylate - PMMA) heat capacity and $C_{p,f}$ the used carbon fibers heat capacity. The polymerization reaction chain is modeled using:

$$\frac{dM}{dt} = -k_p M\sqrt{\frac{2fk_dI}{k_t}} \tag{4}$$

with k_p the coefficient of radical propagation, k_t the one for radical termination and k_d the initiator decomposition steps. The two terms I and f are parameters relative to the reaction initiator, I being the reaction initiator concentration and f the initiator's efficiency factor. f is a fitting parameter, while the parameters k_p, k_t and k_d are computed as described in appendix 1.A of the reference[26]. Another fitting coefficient, γ appears in the calculation of the three mentioned parameters k_p, k_t and k_d. The solution is therefore computed through solving equation 1 through fitting the two parameters (f, γ) to find the most suitable parameters, and the best solution of the problem using the modeling published in [26]., which relies on identifying two fitting parameters (f, γ). The found optimal solutions for $f = 0.5$ and $\gamma = 0.45$, fitted using a Newton gradient descent algorithm, are illustrated in figure 4 for the case of the same two experiments illustrated in figure 3. One should mention that the environment temperature shown in figure 3 is an input for the simulation leading to figure 4. The simulations illustrated in figure 4 assumes an initial degree of polymer conversion $\mathcal{X}_0 = 0$.

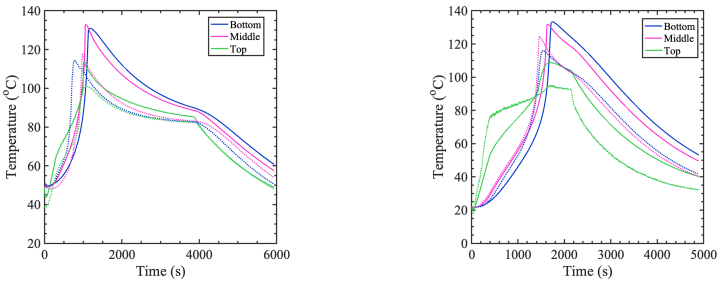

(a) Sample simulation results for experiment 1

(b) Sample simulation results for an experiment 2

Fig. 4: The simulated and the experimentally measured temperatures data for two selected experiments. The dotted lines are the experimental measurements, while the solid lines are the simulation ones.

4.1 Identifying the initial degree of polymer conversion

The solutions using the original modeling published in [26] and illustrated in figure 4 do not allow the prediction of the thermal fields with high fidelity. Since the simulated peak thermal fields are delayed with respect to the experimental ones, while having a higher maximum value, one would imagine that the reaction may have already started in the experimental setting. Therefore, we create a first optimization algorithm to fit 8 parameters, placed in a vector α such as $\alpha = \left(\mathcal{X}_0^1, \mathcal{X}_0^2, \cdots, \mathcal{X}_0^6, f, \gamma\right)$, with $\mathcal{X}_0^i$ is the initial degree of polymer conversion for an experiment i.

Allowing to set $\mathcal{X}_0^i \neq 0$ for experiment i means that the reaction may have already started before the set initial time $t = 0$. An optimization problem is now set to solve the problem parameters through minimizing a cost function J:

$$\alpha^{opt} = \underset{\alpha \in [0,1]^8}{\operatorname{argmin}} \left(J\right), \tag{5}$$

with J being defined as the sum of square errors over all time-steps such as:

$$J = \sum_{i=1}^{6} \int_t \left(T_i^{sim} - T_i^{exp}\right)^2 dt \tag{6}$$

The selected optimization algorithm is the active set optimization algorithm [28], which will identify the 8 parameters by performing the simulation of each experimental setup several times. Active set is suitable for parameters fitted inside a small variation interval, and thus is an appealing gradient descent algorithm for our application [28]. To accelerate the optimization process, a proper orthogonal decomposition (POD) reduced basis is built for the problem a priori, before starting the optimization process [29–32].

4.2 Construction of the reduced order model

A reduced order model based on the POD method is built to accelerate the optimization process. For this aim, the time dependent solution of each available simulation is used to build a POD solution for the corresponding set of the solutions. For instant, we simulate an experimental setting i, considering $\mathcal{X}_0^i = 0, 0.1, 0.2, \cdots, 0.5$, $f = 0.5$ and $\gamma = 0.45$, to obtain a solution $T^i(x,t)$. The solution $T^i(x,t)$ is a matrix of dimension $N \times m$, where N is the number of degrees of freedom in the space domain r and m is the number of time steps. We perform a singular value decomposition (SVD) of $T^i(x,t)$ using:

$$svd(T^i) = \mathbf{U}^i \mathbf{\Lambda}^i \mathbf{W}^i \tag{7}$$

The matrices $\mathbf{U}^i$ and $\mathbf{W}^i$ consists of the space and time mode shapes respectively, while $\mathbf{\Lambda}^i$ is a diagonal matrix containing the singular values of decomposition. The reduced basis $\mathbf{V}^i$ is obtained through retaining only the n highest singular values, and their corresponding vectors in $\mathbf{U}_i$. Noting $\mathbf{V}^i$ the resulting reduced basis, one can write:

$$T^i(x,t) \approx \mathbf{V}^i * \zeta^i(t) \tag{8}$$

where ζ^i is the size n vector of reduced coordinates values in the defined reduced space. One reduced basis is built for every initial degree of polymerization, with an interpolation performed in between the selected values.

Time discretization is performed using and an implicit integration scheme is adopted [33]. At every time step, the discrete form of the problem defined in equation (1) is reduced into a linear system of equations having the form:

$$\mathbf{K}T = \mathbf{B} \tag{9}$$

The projection of equation (9) into the projection reduced basis space leads to:

$$\mathbf{V}^{i^T} \mathbf{K} \mathbf{V}^i \zeta_i = \mathbf{V}^{i^T} \mathbf{B} \tag{10}$$

The equation (10) is therefore reduced to a $n \times n$ system of linear equations instead of $N \times N$ as in equation (9).

Considering the remaining unselected terms of $\mathbf{\Lambda}^i$, one can estimate an error of the POD approximation e_{POD} evaluated on the training snapshots eventually, such as:

$$e_{POD} = \frac{\sum_{j=1}^{j=n_t} \|T_j^i - \mathbf{V}^i \mathbf{V}^{i^T} \mathbf{X} T_j^i\|_{\mathbf{X}}^2}{\sum_{j=1}^{j=n_t} \|T_j^i\|_{\mathbf{X}}^2} = \frac{\sum_{j=1+n}^{j=n_t} {\lambda_j^i}^2}{\sum_{j=1}^{j=n_t} {\lambda_j^i}^2} \tag{11}$$

with n_t the total available snapshots, one per each time step and λ_j^i the diagonal value of matrix $\mathbf{\Lambda}^i$ on line j. The used projection matrix for the inner

product used in this work is the identity matrix, $\mathbf{X} = \mathbf{I}$. The selected value of $n \in [6, 10]$ was used for all the 6 cases, with a POD error $e_{POD} < 10^{-5}$. The final optimization results will also be compared to their final elements counterparts to validate the POD approach.

4.3 Optimized results

The optimization problem defined in equation (5) is coupled to a cost function J evaluation using the reduced basis defined in section 4.2, and solved using an active set algorithm. The convergence leads to $f_{opt} = 0.68$ and $\gamma_{opt} = 0.24$ and an initial degree of polymer conversion $\mathcal{X}_0 \in [0.15; 0.2]$. All the results illustrated in this section are using the material properties shown in A, table 5.

Once the optimal solutions available, the simulation is performed again using finite elements to validate the POD reduced basis, and to alleviate any truncation error generated by the reduced basis. The results are illustrated in figure 5 for two selected simulations.

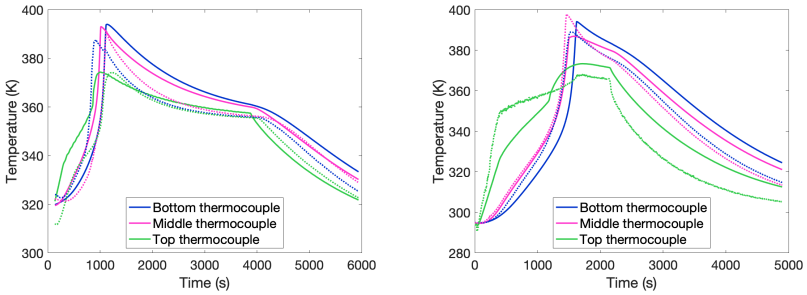

(a) Sample simulation results for an experiment 1

(b) Sample simulation results for an experiment 2

Fig. 5: The simulated thermal field with optimized parameters along with the experimentally measured temperatures for two selected experiments. The dotted lines are the experimental measurements, while the solid lines are the simulation ones.

The results shown in figure 5 show lower relative errors than the ones illustrated in figure 4. However, the shown results are still not fully satisfying and require further enhancement. For this aim, we will combine the obtained optimized simulation to a machine learning algorithm to build a digital twin able to reproduce the experimental results, by enhancing the available simulation through modeling the ignorance, or the error, in the model.

5 Surrogate modeling of the generated error

In this section, we aim to build the digital twin reproducing the error between the simulated results and the experimental ones. First of all, we start by creating a surrogate model to fit the errors $\mathcal{E}_i$ between the simulation and the experimental results, defined as:

$$\mathcal{E}_i = \left(T_i^{exp} - T_i^{sim,opt} \right) \tag{12}$$

The errors are plotted for two selected case in figure 6.

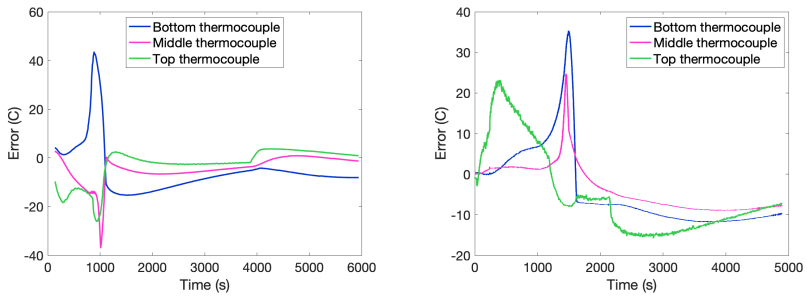

(a) Sample simulation results for an experiment 1

(b) Sample simulation results for an experiment 2

Fig. 6: The relative error between the experimental and simulated results after performing the parametric optimization.

Two modeling methods were used for the surrogate modeling of the error. A first method uses the radial coordinate r as an input, and therefore is able to predict the time-dependent error in all the domain thickness after being trained only on the three available data points. The second method do not uses the r coordinate as an input to the problem, and thus fits only the three available data points. Later on, a parabola is fitted between the available data points to predict the error values in the rest of the thickness domain. In what follows, we detail both methods used for the error modeling.

One should highlight the available data set for training and testing is much larger than the number of experiments. In fact, since transient incremental model is being built, each time step measurement is a data point that can be used in the training of the algorithm. Thus, the total number of available input/output combinations is 26,703 data points, enough to train the considered neural network.

5.1 Considering the radial coordinate as an input parameter

In this part, we use a recurrent neural network with convolution layers to model the error $\mathcal{E}$ between the simulation and the experimental results. We will be omitting the subscript $\cdot_i$ as the error is systematically fitted on five experiments, while the last one is used for testing and evaluation of the fitting quality. The error is approximated as $\tilde{\mathcal{E}}$ by a recurrent convolution neural network, consisting a surrogate model $\mathbf{g}_1$. This model takes as an input the error values in the last 5 time steps on the 3 available thermocouples, the degree of polymer conversion $\mathbf{X}$ estimated on the location of the three thermocouples using the model discussed in section 4, the time t, the radius coordinate of the thermocouple currently being evaluated and the ambient temperature T_{env}. The output is the estimation of the error for the upcoming time step s. For instance one can write:

$$\begin{aligned}\left(\tilde{\mathcal{E}}_s(r)\right) = \mathbf{g}_1 \Bigg(&\begin{pmatrix} \mathcal{E}_{s-1} \\ \vdots \\ \mathcal{E}_{s-5} \end{pmatrix}^{bot}, \begin{pmatrix} \mathcal{E}_{s-1} \\ \vdots \\ \mathcal{E}_{s-5} \end{pmatrix}^{mid}, \begin{pmatrix} \mathcal{E}_{s-1} \\ \vdots \\ \mathcal{E}_{s-5} \end{pmatrix}^{top}, \begin{pmatrix} t_s \\ \vdots \\ t_{s-4} \end{pmatrix}, \\ &\begin{pmatrix} \mathcal{X}_{s-1} \\ \vdots \\ \mathcal{X}_{s-5} \end{pmatrix}^{bot}, \begin{pmatrix} \mathcal{X}_{s-1} \\ \vdots \\ \mathcal{X}_{s-5} \end{pmatrix}^{mid}, \begin{pmatrix} \mathcal{X}_{s-1} \\ \vdots \\ \mathcal{X}_{s-5} \end{pmatrix}^{top}, \begin{pmatrix} T_s \\ \vdots \\ T_{s-4} \end{pmatrix}^{env}, r \Bigg)\end{aligned} \tag{13}$$

The used neural network is illustrated in table 1. The model is trained using 300 epochs and 22506 inputs/outputs combinations, corresponding to all the timesteps from the first 5 experiments, while the validation is performed on the 6^{th} experiment, with 3571 time steps, corresponding to 3567 input/output combinations. All data values are normalized before training. For example, for a data input m, the normalized values m_{norm} are obtained using:

$$m_{norm} = \frac{m - m_{mean}}{m_{max} - m_{min}}, \tag{14}$$

where m_{mean} is the average value of m, m_{max} is the maximum and m_{min} is the minimum value of m. All normalization constants are only computed on the observed in the training set.

The error fittings results are illustrated in table 2, where we represent the mean absolute percentage errors on the observed training and testing sets. The results are not satisfying and therefore the need for the second approach illustrated in section 5.2 is motivated.

Layers	shape	activation
1	2D convolution, 30 filters, kernel (5×4), strides (2×1), no padding	*selu*
2	2D convolution, 60 filters, kernel (1×3), strides (1×3), no padding	*selu*
3	A flatten layer, reshapes all inputs into a single vector	no activation
4	Fully connected dense layer with 1200 neurons	*selu*
5	Fully connected dense layer with 500 neurons	*selu*
8	Fully connected dense layer with 1 neuron	*linear*

Table 1: Structure of the deep convolution neural network $\mathbf{g}_1$ used for the fitting of $\tilde{\mathcal{E}}$. *selu* stands for the scaled exponential linear unit [34], while *linear* stands for linear activation or no activation function.

Model $\mathbf{g}_1$	Mean absolute percentage error	Root mean square error (^{o}C)
Training sets	23%	0.4607
Testing sets	45%	0.3862

Table 2: Mean relative errors of the trained model $\mathbf{g}_1$

5.2 Modeling only the available data points with a parabolic fitting in-between

In this part, we approximate again $\tilde{\mathcal{E}}$ by a recurrent convolution neural network, consisting a surrogate model $\mathbf{g}_2$. This model does not take as an input the radius location r, but still takes as an input the error values in the last 3 time steps on the 3 available thermo couples, the degree of polymer conversion $\mathbf{X}$ estimated on the location of the three thermo couples using the model discussed in section 4, the time t and the ambient temperature T_{env}. The output is the estimation of the error for the upcoming time step s on the three available thermocouples. For instance we can write:

$$\left(\tilde{\mathcal{E}}_s^{\,bot}, \tilde{\mathcal{E}}_s^{\,mid}, \tilde{\mathcal{E}}_s^{\,top}\right) = \mathbf{g}_2 \left(\begin{pmatrix} \mathcal{E}_{s-1} \\ \vdots \\ \mathcal{E}_{s-3} \end{pmatrix}^{bot}, \begin{pmatrix} \mathcal{E}_{s-1} \\ \vdots \\ \mathcal{E}_{s-3} \end{pmatrix}^{mid}, \begin{pmatrix} \mathcal{E}_{s-1} \\ \vdots \\ \mathcal{E}_{s-3} \end{pmatrix}^{top}, \begin{pmatrix} t_s \\ \vdots \\ t_{s-2} \end{pmatrix}, \begin{pmatrix} \mathcal{X}_{s-1} \\ \vdots \\ \mathcal{X}_{s-3} \end{pmatrix}^{bot}, \begin{pmatrix} \mathcal{X}_{s-1} \\ \vdots \\ \mathcal{X}_{s-3} \end{pmatrix}^{mid}, \begin{pmatrix} \mathcal{X}_{s-1} \\ \vdots \\ \mathcal{X}_{s-3} \end{pmatrix}^{top}, \begin{pmatrix} T_s \\ \vdots \\ T_{s-2} \end{pmatrix}^{env} \right) \tag{15}$$

The used neural network is illustrated in table 3. The model is trained using 2500 epochs using the same data combinations illustrated in section 5.1. However, in this case, not each sensor consists a data set by its own, therefore the number of available combinations is divided by 3, as each 3 thermocouples consists a single input/output combination. All data values are normalized before training using the same approach as in section 5.1.

Layers	shape	activation
1	2D convolution, 30 filters, kernel (3×4), strides (3×1), no padding	*selu*
2	2D convolution, 60 filters, kernel (1×2), strides (1×2), no padding	*selu*
3	A flatten layer, reshapes all inputs into a single vector	no activation
4	Fully connected dense layer with 1200 neurons	*selu*
5	Fully connected dense layer with 50 neurons	*selu*
8	Fully connected dense layer with 3 neuron	*linear*

Table 3: Structure of the deep convolution neural network $\mathbf{g}_2$ used for the fitting of $\tilde{\mathcal{E}}$. *selu* stands for the scaled exponential linear unit [34], while *linear* stands for linear activation or no activation function.

The error fittings results are illustrated figure 7 for two selected experiments, while the table 4 represents the mean absolute percentage errors on the observed training and testing sets. It is clear that, although the used network does not take the radius into consideration, it performs much better than the one illustrated in section 5.1, and therefore this approach will be adopted for the digital twin construction.

The model $\mathbf{g}_2$ outperforms $\mathbf{g}_1$, as it doesn't has to predict the through thickness variation of the results, as it is fitted using the parabolic variations. In fact, with only 3 available measurements through the thickness dimension, and absence of any other information about the discrepancy, a parabolic estimation is the most suitable approach.

Model $\mathbf{g}_2$	Mean absolute percentage error	Root mean square error (^{o}C)
Training sets	7.9%	0.1765
Testing sets	13.25%	0.1463

Table 4: Mean relative errors of the trained model $\mathbf{g}_2$

6 Digital twin results

In this section we combine the solution obtained from the optimized simulation, to the one obtained from the recurrent neural network, building therefore a digital twin of the thermal solution. The final digital twin thermal solution T^{DT} is computed as:

$$T^{DT} = T^{sim} + \tilde{\mathcal{E}} \tag{16}$$

The digital twin solution of the thermal fields is illustrated in figure 8 for a selected testing and training experiments. The comparison with the experimental thermal results is illustrated in figure 9. Later on, the thermal fields are leveraged to compute the resin polymerization degree $\mathcal{X}$, using the model proposed in [26]. The results are illustrated in figure 10 for selected experimental testing and training set.

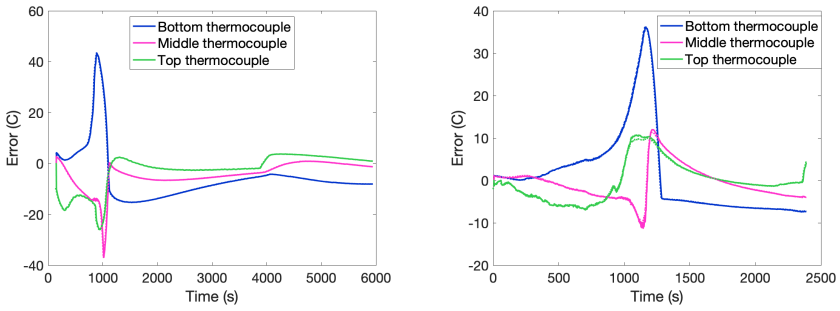

(a) $\mathbf{g}_2$ training results (b) $\mathbf{g}_2$ testing results

Fig. 7: Sample results of $\mathbf{g}_2$ surrogate model for the training data-set of experiment 2 and for the testing data-set, experiment 6. The dotted lines are the correct errors obtained in equation (12), while the solid lines are the neural network output

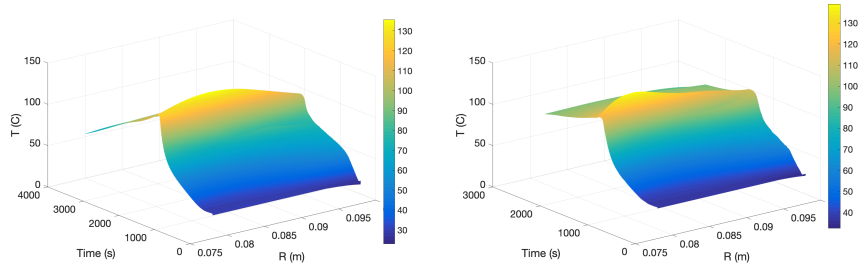

(a) $\mathbf{g}_2$ final digital twin training results (b) $\mathbf{g}_2$ final digital twin testing results

Fig. 8: Sample results of $\mathbf{g}_2$ surrogate model combined with the simulation data.

7 Conclusion

In this work, we developed a digital twin of the in-situ polymerization of a cylindrical continuous fiber composite material, impregnated with Elium®resin. Elium®is a reactive resin with auto-accelerating polymerization kinetics. The simulation obtained using the implemented digital twin is of high predictive ability, validated on an experimental set never seen during the training. The obtained model is leveraged through post processing the degree of resin polymerization through the thickness of the part and the processing time. The described procedure allows therefore to predict the ability of the monomers to react and polymerize leading to the final desired part, while avoid local overheating and degradation of the Elium®matrix.

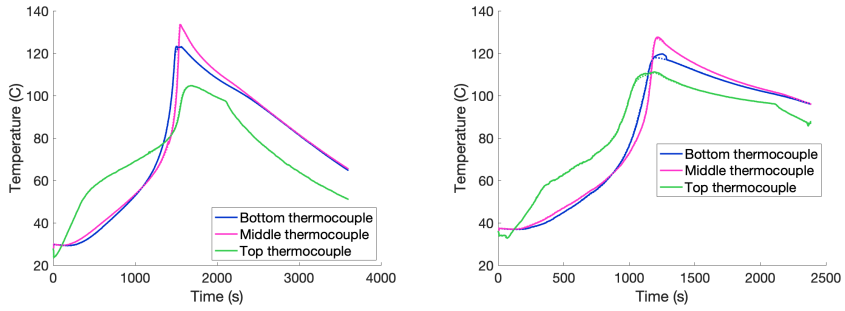

(a) $\mathbf{g}_2$ final digital twin training results (b) $\mathbf{g}_2$ final digital twin testing results

Fig. 9: Sample results of $\mathbf{g}_2$ surrogate model combined with the simulation data. The dotted lines are the experimental measurements, while the solid lines are the digital twin output

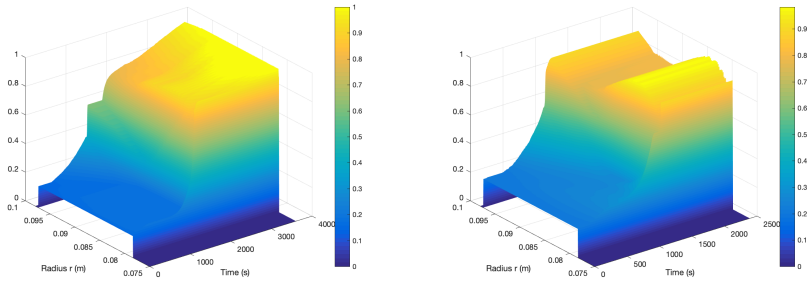

(a) Post processing the degree of resin polymerization in a training experiment (b) Post processing the degree of resin polymerization in a testing experiment

Fig. 10: Post processing of the digital twin output to compute the final degree of monomer conversion

Acknowledgements. This work was proposed in the framework of the E2S UPPA AWESOME Chair. The authors would like to thank the Chair partners (E2S UPPA, ARKEMA and CANOE) for funding their work.

Compliance with Ethical Standards. The authors declare that they have no conflict of interest.

A Polymerization material properties

In this section we review the used properties of the polymerized composite material, as illustrated in table 5. For detailed explanation on the used polymerization and heat generation model please refer to reference [26], appendix A.

Properties	Values
Tape thickness	0.215 mm
Cylindrical support thickness	3 mm
Mesh distance between nodes	43 μm
Time step Δt	1 s
Initiator decomposition energy	124000 J/mol
Initiator pre-exponential factor for macro-radical diffusion	3×10^{-6} m^2/s
Overlap factor γ_m	0.8
Overlap factor of macroradical γ_t	1.8
Normalized initiator diffusion coefficient	12.5
Initial air temperature T_0	25^oC
Mass fraction of the resin in the composite	0.25
Thermal diffusivity of the mold	90×10^{-6} m^2/s
Thermal conductivity of the mold	100 $W/m.K$
Thermal diffusivity of the composite	2.0815×10^{-7} m^2/s
Thermal conductivity of the composite	0.7 $W/m.K$
Resin molecular weight	0.100121 kg/mol
Polymerization enthalpy	57800 J/mol
Activation energy of propagation step	22360 J/mol
Activation energy of termination step	5890 J/mol
Pre-exponential factor of propagation step	2670 $m^3.kg.mol/s$
Pre-exponential factor of termination step	198 400 $m^3.kg.mol/s$
Pre-exponential factor of initiator decomposition step	7.44×10^{15} s^{-1}
Coefficient of chain transfer to monomer	5×10^{-5}
Coefficient of chain transfer to initiator	6×10^{-2}
Interaction radius of propagation step	2.93×10^{-10} m
End-to-end distance per square root of number of monomer units in chain	6.9×10^{-10} m
Average entanglement spacing in polymer	70
Pre-exponential factor for calculation of monomer diffusion coefficient	3×10^{-8} m^2/s
Glass transition temperature of monomer	-126^oC
Glass transition temperature of polymer	114^oC
Density of monomer	$940kg/m^3$
Density of polymer	$1170kg/m^3$

Table 5: Material and simulation properties used in for optimization problem detailed in section 4

References

1. H. P. Kumar, M. A. Xavior, Composite materials production for automobile applications, in: D. Brabazon (Ed.), Encyclopedia of Materials: Composites, Elsevier, Oxford, 2021, pp. 640–651. doi:https://doi.org/10.1016/B978-0-12-803581-8.11894-6.
URL `https://www.sciencedirect.com/science/article/pii/B9780128035818118946`
2. M. Perez, A. Barasinski, B. Courtemanche, C. Ghnatios, F. Chinesta, Sensitivity thermal analysis in the laser assisted tape-placement process, Aims Materials Science 5 (6) (2018) 1053–1072. doi:10.3934/matersci.2018.6.1053.
3. R. Stewart, Thermoplastic composites - recyclable and fast to process, Reinforced Plastics 55 (3) (2011) 22–28. doi:https://doi.org/10.1016/S0034-3617(11)70073-X.
URL `https://www.sciencedirect.com/science/article/pii/S003436171170073X`
4. R. Bernatas, S. Dagreou, A. Despax-Ferreres, A. Barasinski, Recycling of fiber reinforced composites with a focus on thermoplastic composites, Cleaner Engineering and Technology 5 (2021) 100272.
5. R. Jones, Mechanics of composite materials, 2nd Edition, Taylor and Francis group, 1999.

6. N. Bur, P. Joyot, C. Ghnatios, P. Villon, E. Cueto, F. Chinesta, On the use of model order reduction for simulating automated fibre placement processes, Advanced Modeling and Simulation in Engineering Sciences 3 (2016) 1–18. doi:10.1186/s40323-016-0056-x.
7. S. Strau, F. Wilhelm, Development of a flexible injection and impregnation chamber for pultrusion of high reactive resins, Procedia Manufacturing 47 (2020) 956–961, 23rd International Conference on Material Forming. doi:https://doi.org/10.1016/j.promfg.2020.04.294.
   URL https://www.sciencedirect.com/science/article/pii/S2351978920313603
8. C. Ghnatios, P. Simacek, F. Chinesta, S. Advani, A non-local void dynamics modeling and simulation using the proper generalized decomposition, International Journal of material fomring 13 (2020) 533–546.
9. F. Castéran, R. Ibanez, C. Argerich, K. Delage, F. Chinesta, P. Cassagnau, Application of machine learning tools for the improvement of reactive extrusion simulation, Macromolecular Materials and Engineering 12 (2020) 2000375.
10. A. Adel, khaled Salah, Model order reduction using artificial neural networks, in: 2016 IEEE International Conference on Electronics, Circuits and Systems (ICECS), IEEE, 2016, pp. 89–92.
11. B. V. de Weg, L. Greve, M. Andres, T. Eller, B. Rosic, Neural network-based surrogate model for a bifurcating structural fracture response, Engineering Fracture Mechanics 241 (2021) 107424.
12. R.-M. Hage, I. Hage, C. Ghnatios, I. Jawahir, R. Hamade, Optimized tabu search estimation of wear characteristics and cutting forces in compact core drilling of basalt rock using pcd tool inserts, Computers & industrial engineering 136 (10) (2019) 477–493.
13. C. Ghnatios, R.-M. Hage, I. Hage, An efficient tabu-search optimized regression for data-driven modeling, Compte rendu mecanique 347 (11) (2019) 806–816.
14. R. Xu, N. Wang, D. Zhang, Solution of diffusivity equations with local sources/sinks and surrogate modeling using weak form theory-guided neural network, Advances in water resources In press (2021). doi:https://doi.org/10.1016/j.advwatres.2021.103941.
15. R. Ibanez, F. Casteran, C. Argerich, C. Ghnatios, N. Hascoet, A. Ammar, P. Cassagnau, F. Chinesta, On the data-driven modeling of reactive extrusion, Fluids 94 (5) (2020) 1–23. doi:10.3390/fluids5020094.
16. D. González, F. Chinesta, E. Cueto, Thermodynamically consistent data-driven computational mechanics, Contin. Mech. Thermodyn. 31 (2019) 239–253.
17. C. Ghnatios, I. Alfaro, D. Gonzalez, F. Chinesta, E. Cueto, Data-driven generic modeling of poroviscoelastic materials, Entropy 21 (12) (2019) 1165.
18. D. Gonzalez, F. Chinesta, E. Cueto, Thermodynamically consistent data-driven computational mechanics, Continuum mechanics and thermodynamics 31 (1) (2019) 239–253.
19. C. Soize, A nonparametric model of random uncertainties for reduced matrix models in structural dynamics, Probabilistic Engineering Mechanics 15 (3) (2000) 277–294.
20. C. Soize, C. Farhat, A nonparametric probabilistic approach for quantifying uncertainties in low- and high-dimensional nonlinear models, International Journal for Numerical methods in engineering 109 (2016) 837–888. doi:10.1002/nme.5312.
21. C. Farhat, A. Bos, P. Avery, C. Soize, Modeling and quantification of model-form uncertainties in eigenvalue computations using a stochastic reduced model, American Institute of Aeronautics and Astronautics Journal 56 (3) (2017) 1–22.
22. C. Soize, C. Farhat, Probabilistic learning for modeling and quantifying model-form uncertainties in nonlinear computational mechanics, International Journal for Numerical methods in engineering 117 (2019) 819–843. doi:10.1002/nme.5980.
23. F. Chinesta, E. Cueto, E. Abisset-Chavan, J.-L. Duval, F. Khaldi, Virtual, digital and hybrid twins: A new paradigm in data-based engineering and engineered data, Archives of Computational Methods in Engineering 27 (2020) 105–134.
24. C. Ghnatios, A hybrid modeling combining the proper generalized decomposition (pgd) approach to data-driven model learners, with application to non-linear biphasic materials, Comptes rendus mécanique In Press (2021).
25. C. Ghnatios, A. Barasinski, A nonparametric probabilistic method to enhance pgd solutions with data-driven approach, application to the automated tape placement process, Advanced Modeling and Simulation in Engineering Sciences 8 (1) (2021) 20. doi:10.1186/s40323-021-00205-5.
   URL https://doi.org/10.1186/s40323-021-00205-5

26. S. Gayot, C. Bailly, T. Pardoen, P. Gérard, F. V. Loock, Processing maps based on polymerization modelling of thick methacrylic laminates, Materials and Design 196 (2020) 109170.
27. D. Askeland, P. Fulay, W. Wright, The Science and Engineering of Materials, 6th Edition, Cengage Learning, 2020.
28. J. Nocedal, S. J. Wright, Numerical Optimization, Springer, 1999.
29. C. Allery, C. Beghein, A. Hamdouni, Applying proper orthogonal decomposition to the computation of particle dispersion in a two-dimensional ventilated cavity, Communications in Nonlinear Science an Numerical Simulation 10 (2005) 907–920.
30. E. Liberge, A. Hamdouni, Reduced order modelling method via proper orthogonal decomposition (pod) for flow arround and oscillating cylinder, Journal of Fluid and Structures 26 (2010) 292–311.
31. D. Ryckelynck, A priori hyper-reduction method : An adaptive approach, Journal of Computational Physics 202 (2005) 346–366.
32. C. Bernardi, Y. Maday, Spectral methods, Handbook of Numerical Analysis 5 (1997) 209–485.
33. J. Reddy, An introduction to the finite element method, 3rd Edition, Mc Graw Hill, 2006.
34. G. Klambauer, T. Unterthiner, A. Mayr, Self-normalizing neural networks, in: 31st Conference on Neural Information Processing Systems (NIPS 2017), Long Beach, CA, USA, 2017, pp. 1–102.